Dalton Transactions

ROYAL SOCIETY
OF CHEMISTRY

PAPER
M. Ruben and co-workers
Bi-stable spin-crossover in charge-neutral [Fe(R-ptp)₂]
(ptp = 2-(1H-pyrazol-1-yl)-6-(1H-tetrazol-5-yl)pyridine)
complexes

PAPER

Check for updates

Bi-stable spin-crossover in charge-neutral [Fe(R-ptp)₂] (ptp = 2-(1H-pyrazol-1-yl)-6-(1H-tetrazol-5-yl)pyridine) complexes†

Kuppusamy Senthil Kumar, [ID] *[a] Sergi Vela, [ID] *‡[b] Benoît Heinrich, [ID] [a] Nithin Suryadevara,[c] Lydia Karmazin, [ID] [d] Corinne Bailly[d] and Mario Ruben [ID] *[a,c]

Bi-stable charge-neutral iron(II) spin-crossover (SCO) complexes are a class of switchable molecular materials proposed for molecule-based switching and memory applications. In this study, we report on the SCO behavior of a series of iron(II) complexes composed of rationally designed 2-(1H-pyrazol-1-yl)-6-(1H-tetrazol-5-yl)pyridine (ptp) ligands. The powder forms of $[Fe^{2+}(R-ptp^-)_2]^0$ complexes tethered with less-bulky substituents—R = H (**1**), R = CH_2OH (**2**), and R = $COOCH_3$ (**3**; previously reported)—at the 4-position of the pyridine ring of the ptp skeleton showed abrupt and hysteretic SCO at or above room temperature (RT), whereas complex **5** featuring a bulky pyrene substituent showed incomplete and gradual SCO behavior. The role of intermolecular interactions, lattice solvent, and electronic nature of the chemical substituents (R) in tuning the SCO of the complexes is elucidated.

Introduction

Spin-crossover (SCO) active transition metal complexes capable of undergoing hysteretic spin-state switching, upon application of external stimulus such as temperature or light, between the low spin (LS) and the high spin (HS) states or *vice versa* at or around room temperature (RT)[1–11] are promising candidates to fabricate molecule-based electronics and spintronics devices.[12–20] Factors such as ligand field strength, nature of counter anions, lattice solvent/guest molecules, and

intermolecular interactions govern SCO.[21,22] The ligand field strength could be modulated by a careful ligand design strategy, as exemplified by the substituent dependence of spin-state switching in the solid[23,24] and solution phases.[25–32] Spin-crossover is accompanied by bond length alteration (Δr) with concomitant volume change (ΔV).[33–36] In solution, the lack of intermolecular interactions manifests as a gradual SCO transition that is not useful for materials applications.[37–40] On the contrary, in the solid-state, the aforementioned structural rearrangements generate cooperativity, leading to abrupt- or even hysteretic-transitions when cooperativity is strong enough.[41–54] Consequently, the SCO of metal centres is often investigated in the solid-state to harness SCO-based applications. Although crystal engineering approaches[8,55–62] have been proposed, having strict control over intermolecular interactions in the crystal lattice of an SCO complex is difficult to achieve and a complex phenomenon to model.[63] The synthesis of counter-anion free charge-neutral complexes simplifies the problem to an extent and allows one to focus more on the role of intermolecular interactions between the switching entities. It is reported that a more organized molecular environment in a crystal lattice blocks the occurrence of the SCO because lattice constraints inhibit the structural reorganizations accompanying the SCO.[34,63–65] On the other hand, there is no general rule of how lattice solvent molecules affect the SCO, and the effect of solvent on the SCO behavior is case dependent.[55,66–72] In short, a favourable crystallographic environment composed of appropriate intermolecular contacts and presence or absence of lattice guest(s) seems to govern the

[a]*Institut de Physique et Chimie des Matériaux de Strasbourg (IPCMS), CNRS-Université de Strasbourg, 23, rue du Loess, BP 43, 67034 Strasbourg Cedex 2, France. E-mail: senthil.kuppusamy@ipcms.unistra.fr*

[b]*Laboratoire de Chimie Quantique, Institut de Chimie, UMR 7177 CNRS-Université de Strasbourg, 4 rue Blaise Pascal, 67081 Strasbourg, France. E-mail: sergi.vela@gmail.com*

[c]*Institute of Nanotechnology (INT), Karlsruhe Institute of Technology (KIT), Hermann-von-Helmholtz-Platz 1, 76344 Eggenstein-Leopoldshafen, Germany. E-mail: mario.ruben@kit.edu*

[d]*Service de Radiocristallographie, Fédération de Chimie Le Bel, FR2010 CNRS-Université de Strasbourg, 1 rue Blaise Pascal, BP 296/R8, 67008 Strasbourg Cedex, France*

occurrence and nature of spin-state switching of an iron(II) complex.

Charge-neutral complexes are potential candidates to analyse SCO from the above discussed perspective and to obtain spin-state switching suitable for applications.[73,74] In this context, we have developed a new family of charge-neutral iron(II) complexes based on pyrazol-1-yl-6-(1H-tetrazol-5-yl)pyridine (ptp) ligand[6] and studied the SCO of two [Fe(R-ptp)$_2$] complexes—[Fe(L^1)$_2$] (**1**) and [Fe(L^3)$_2$] (**3**) (Chart 1). Complex **1** in its crystalline form showed bi-stable SCO with $T_{1/2}$ = 295 K and ΔT = 5 K.[6] The powder form of complex **3** showed above RT SCO with $T_{1/2}$ = ~348 K and ΔT = ~3 K, whereas the corresponding crystalline complex remained LS until 385 K.[75] The utility of **1** as a solvent sensor[76] and the ability of the complex to modulate spin-polarized transport[77] in a single-molecule junction has been demonstrated. The lanthanoid (Eu^{3+} and Tb^{3+}) luminescence sensitizing ability of ptp ligand systems, namely, L^{1-} and L^{3-} has also been reported,[78] elucidating the usefulness of the ligands to construct functional charge-neutral transition metal and lanthanoid complexes.

To systematically explore structure–SCO property relationships in [Fe(R-ptp)$_2$] complexes, three new charge-neutral complexes—**2**, **4**, and **5** (Chart 1)—were synthesized; pyrene teth-

ered complex **5** could also serve as an useful model to study spin-state dependent conductance switching in single-molecule junctions.[79] In the following sections, SCO of the newly synthesized complexes, along with the SCO behavior of the previously reported complexes (**1** and **3**), are discussed to elucidate factors governing spin-state switching in the [Fe(R-ptp)$_2$] family of complexes.

Results and discussion

Synthesis of the ligands and the complexes

The precursor ligand L^{4}H was obtained from 2,6-dibromopyridine-4-carboxylic acid (Scheme S1†), and the ligands L^{n}H (n = 2 and 5) were synthesized from L^{4}H as depicted in Scheme 1.

The syntheses of complexes **1** (in crystalline form) and **3** (in crystalline and powder forms) were reported in our previous studies.[6,75] To make comparisons meaningful, **1** was synthesized in powder form as detailed in the ESI.† Dark-red block single crystals of **4** suitable for X-ray diffraction (XRD) were obtained by performing the complexation reaction under dilute condition (Scheme 1, (c) condition 1) and allowing the mother liquor to stand under ambient conditions for a period of 2–3 weeks. Under similar conditions, about 3 mg of crystalline solids were obtained for **2**, and the crystals were found to be too small for X-ray structure determination. The powder form of complexes **2** and **4** were obtained by performing the complexation reactions in CH$_2$Cl$_2$/MeOH solvent mixture using relatively concentrated ligand solutions (Scheme 1, (c) condition 2). The pyrene tethered complex **5** was obtained by treating Fe(II) salt with the corresponding ligand solution in CH$_2$Cl$_2$/MeOH solvent mixture. Attempts to crystallize **5** from CH$_2$Cl$_2$/MeOH solvent mixture were not successful. However,
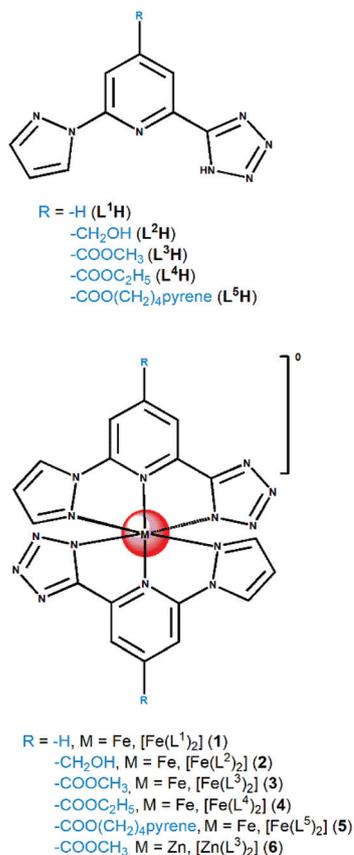
Chart 1 Molecular structures of PTP ligands (top) and the corresponding Fe(II) and Zn(II) complexes (bottom). The complexes **2**, **4**, **5**, and **6** are newly reported in this study.
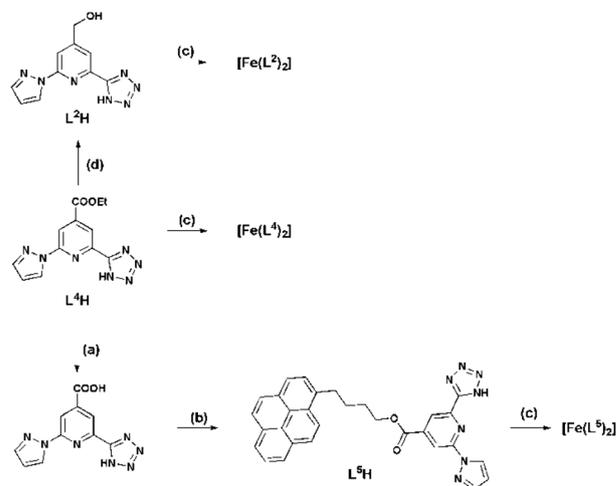
Scheme 1 Synthesis of ligands L^{n}H (n = 2 and 5) and complexes [Fe(L^n)$_2$] (n = 2 and 4–5). Reagents and conditions: (a) KOH, H$_2$O, reflux, overnight, (b) DCC/DMAP, CH$_2$Cl$_2$, RT, 24 h, (c) Condition 1: CH$_2$Cl$_2$ (21 mL)/MeOH (9 mL), Et$_3$N, Fe(BF$_4$)$_2$·6H$_2$O, RT, 2 h or condition 2: CH$_2$Cl$_2$ (7 mL)/MeOH (3 mL), Et$_3$N, Fe(BF$_4$)$_2$·6H$_2$O, RT, 24 h, and (d) NaBH$_4$, EtOH, reflux, 12 h.

slow evaporation of a saturated solution of **5** in 1,2-dichloro-benzene/MeOH solvent mixture yielded a few crystals suitable for X-ray analysis, which helped us to elucidate the molecular structure of **5** as detailed in the following section. Photophysical characteristics of the newly synthesized ligands and complexes are discussed in the ESI; see Fig. S1 and S2.†

Crystallographic analyses

Single crystal X-ray diffraction analysis of **4** performed at 173 K revealed the crystallization of the complex in monoclinic crystal system with *C*2/*c* space group and absence of lattice solvents (crystallographic data in Table S1†). A coordination number of six was obtained with three nitrogen atoms from each ligand donating electron density to iron(II) in a slightly distorted octahedral coordination geometry, as shown in Fig. 1a.

The asymmetric unit contains half a molecule of **4**, the Fe atom being on the inversion centre. The unit cell contains four complex units. The average Fe–N bond length of 1.93(4) Å and angular parameters listed in Table 1 indicate the LS state of **4** at 173 K. Intermolecular contacts involving H5 (pyridine)⋯N5 (tetrazole) (*d* = 2.42 Å) and N6 (tetrazole)⋯H3 (pyrazole) (*d* = 2.28 Å) atoms are observed in the crystal lattice of **4** as shown in Fig. 1(b).
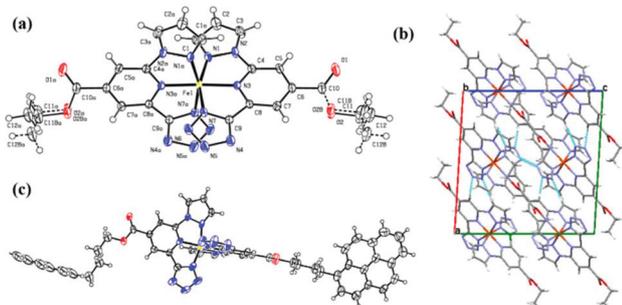
Fig. 1 (a) ORTEP diagram of **4** (CCDC 1839481†) at 50% probability level, (b) unit cell packing pattern of **4** viewed down crystallographic *b* axis; intermolecular interactions are represented with dotted lines, and (c) ORTEP diagram of **5** (CCDC 1407913†) at 50% probability level. Symmetry transformation used to generate equivalent atoms—**4**: #1 − *x* + 2, *y*, −*z* + 3/2, and **5**: *x*, *y*, *z* and −*x*, −*y*, −*z*.

Complex **5** crystallized with methanol solvent in the triclinic crystal system with *P*1̄ space group (crystallographic data in Table S2†). The asymmetric unit contains one molecule of **5** and one molecule of methanol hydrogen-bonded to tetrazole nitrogen (Fig. S3(a)†). The structure is correct with *R* = 8.60; however, alkyl and pyrene segments of one of the ligands are disordered. The π–π interactions between the disordered pyrene segments form an interlayer between successive layers of the regularly arranged complexes, conferring a lamellar character to the structure (Fig. S3(b)†). The bond lengths and angular parameters collected in Table 1 revealed LS state of complex **5** at 173 K.

Structure–property relationships in Fe(II) complexes, especially in [Fe(R-bpp)$_2$]$^{2+}$ (bpp = 2,6-di(1*H*-pyrazol-1-yl)pyridine) family of complexes, have been elucidated by analysing the variations in bond lengths and angular parameters of complexes in their LS and HS states.[34] To get insights into the shape of [Fe(R-ptp)$_2$] complexes and the nature of coordination environment around iron(II) in the complexes, the bond lengths and angular parameters of complexes **1**, **3**, **4** and **5** are collected in Table 1. Comparable values of Fe–N bond lengths, N(pyrazole)–Fe–N(tetrazole) clamp angle (ψ), and an average of four *cis*-N–Fe–N bite angles (α) are obtained for all the complexes. A smaller *trans*-N(pyridine)–Fe–N(pyridine) bond angle (ϕ) = 173.6(7)° is observed for **3** relative to the ϕ values observed for complexes **1**, **4**, and **5**. This signifies the slightly more rotated nature of one of L^{3-} with respect to the other about the iron(II) centre. The dihedral angle (θ) between the planes of the two ligands is smaller in **4** relative to other complexes, indicating more twisted nature of plane corresponding to one ligand about its Fe–N(pyridine bond) with respect to the plane corresponding to another ligand in **4**. While the parameters θ and ϕ are a measure of the shape of a complex, the distortion parameter Σ ($\sum = \sum_{i=1}^{12} |90 - \alpha i|$; α = twelve *cis*-N–Fe–N angles) is a measure of coordination geometry/ligand field environment around the central iron(II). A perfectly ideal octahedral complex shows $\Sigma = 0$, whereas distorted complexes show Σ values in the range of 90° and 160° for the LS and HS complexes, respectively. A slightly distorted nature of complexes **1**, **3**, **4**, and **5** are inferred from the Σ values listed in Table 1. Further, the angular parameters of LS-[Fe(R-ptp)$_2$]

Table 1 Bond lengths and angular parameters—ϕ, ψ, Σ, θ, and α—of the complexes discussed in this study

Parameter	1	3	4	5	6
Temperature/K	180	180	173	173	173
M^a–N(pyridine)/Å	1.91(7)	1.90(2)	1.90(1)	1.902(7)	2.11(0)
M–N(pyrazole)/Å	1.95(4)	1.95(5)	1.96(1)	1.963(7)	2.24(6)
M–N(tetrazole)/Å	1.96(9)	1.94(2)	1.95(1)	1.953(5)	2.13(3)
N(pyridine)–M–N(pyridine) (ϕ)/°	177.4(7)	173.6(7)	177.3(2)	178.38(15)	166.8(9)
N(pyrazole)–M–N(tetrazole) (ψ)/°	160.3(8)	160.3(8)	160.3(1)	160.42(13)	150.0(1)
Σ/°	87.1(8)	85.0(3)	89.6(5)	86.2(9)	135.03(8)
θ/°	89.7(5)	86.9(3)	82.5(1)	86.51(5)	89.77
α/°	79.9(8)	80.2(2)	80.2(1)	80.2(3)	74.99(5)

^{a} M = Fe for **1**, **3**, **4**, and **5** and M = Zn for **6**.

complexes—**1**, **3**, **4**, and **5**—collected in Table 1 is of comparable magnitude reported for the analogous LS-[Fe(1-bpp)$_2$] complexes,[80] indicating similar coordination geometry associated with both family of complexes. A complete elucidation of structure SCO property relationships in [Fe(R-ptp)$_2$] complexes requires crystallographic data of HS-[Fe(R-ptp)$_2$] complexes, which have eluded our grasp so far.

This experimental gap could be tentatively filled by considering the X-ray structure of [Zn(L^3)$_2$]·MeOH (**6**) as a structural mimic of HS-[Fe(L^3)$_2$]: the similar ionic radius of HS-Fe(II) and Zn(II) ions facilitates such a comparison.[81] The structural parameters of **6** are collected in Tables 1 and S3.† The X-ray structure of **6** depicted in Fig. S4† indicates a distorted coordination environment ($\Sigma = \sim 135°$) around Zn(II) analogous to the observations made for HS-[Fe(R-bpp)$_2$]$^{2+}$ family of complexes.[34,82] A reduced $\phi = 166.8(9)°$ observed for **6**, relative to complexes **1**, **3**, **4**, and **5**, indicates more rotated nature of one of L^{3-} with respect to the other about the Zn(II) centre. The dihedral twist (θ) = 89.77° reveals the absence of twist between the planes corresponding to the L^{3-} ligands. The continuous shape measure (CShM)[83] values of the complexes **1** (2.07), **3** (2.09), **4** (2.04), and **5** (1.99) indicate a slightly deviated nature of the coordination polyhedra from the ideal octahedron (O$_h$). A CShM value of 4.85 obtained for complex **6** (HS-mimic) evidences a relatively more distorted nature of the HS-polyhedron in comparison with its LS counterparts. In short, a relatively more distorted coordination environment around Fe(II), and rotation of one ligand with respect to the other is envisioned for the HS-[Fe(R-ptp)$_2$] complexes relative to their LS counterparts.

Spin-state switching behavior of the complexes

The previously reported crystalline complex **1** showed bi-stable SCO ($T_{1/2} = \sim 295$ K and $\Delta T = \sim 5$ K). On the other hand, the powder form of –COOMe substituted complex **3** exhibited above-RT SCO ($T_{1/2} = \sim 348$ K and $\Delta T = \sim 3$ K), whereas the lattice solvent-free crystalline form of **3** remained LS until 400 K. The newly reported complexes **2**, **4**, and **5** were all obtained in powder form, and complex **4** was obtained both in crystalline and powder forms. To facilitate comparisons between the SCO behavior among the complexes, complex **1** was prepared in powder form, which showed bi-stable SCO, like its crystalline counterpart, with $T_{1/2} = \sim 296$ K and $\Delta T = 7$ K as depicted in Fig. 2a. The powder form of complex **2** also underwent an abrupt SCO with $T_{1/2} = \sim 301$ K and $\Delta T = 5$ K as shown in Fig. 2b; $\chi_m T$ product of 3.3 cm^3 K mol^{-1} and 0.11 cm^3 K mol^{-1} at 385 K and 5 K, respectively, indicates a genuine temperature-induced SCO. Conversely, the powder form of **4** showed $\chi_m T$ product of 0.3 cm^3 K mol^{-1} and 0.75 cm^3 K mol^{-1} at 5 K and 385 K, respectively (Fig. 2b) indicating predominantly LS character of it along with a small remnant HS fraction. The lattice solvent-free crystalline sample of complex **4** is diamagnetic until 385 K analogous to **3**.

Note the slight downslope in the ~ 275 K–75 K temperature range for **2** that follows a steeper variation of the $\chi_m T$ product below ~ 75 K. The downslope likely reveals the presence of a
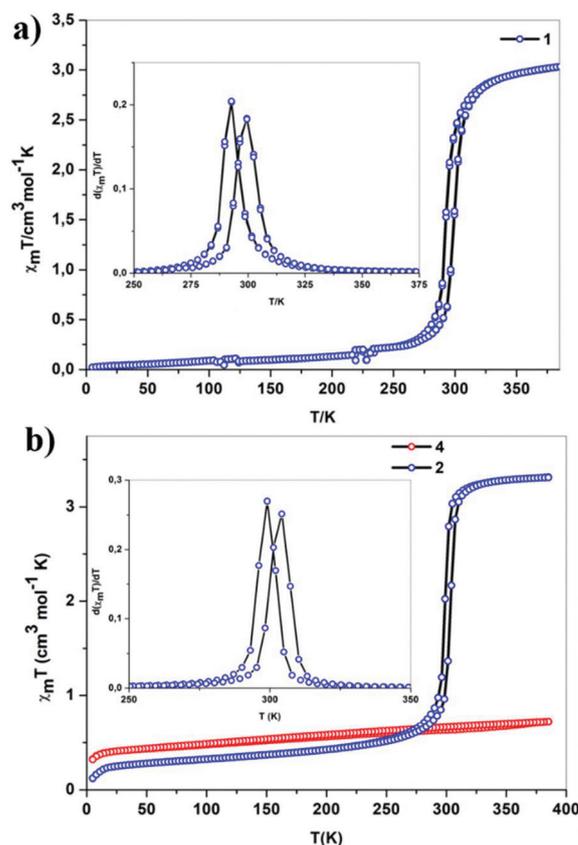
Fig. 2 $\chi_M T$ versus T plots of powder forms of (a) **1** and (b) **2** and **4**. The insets show the d($\chi_M T$)/dT versus T plots of **1** and **2**. The second stable heat-cool cycles (**1** and **2**) obtained at a scan rate of 1 K min^{-1} are shown.

remnant HS fraction of complex **2** below the main SCO region and its gradual switching to LS state on decreasing temperature. The steeper variation below ~ 75 K is attributed to the depopulation of zero field split (ZFS) excited levels of the HS term ^{5}T$_g$.

The pyrene tethered complex **5** is LS at 300 K and underwent incomplete SCO upon heating with the onset of spin-state switching around 350 K as shown in Fig. S5.†

Differential scanning calorimetry (DSC) and variable temperature small- and wide-angle X-ray scattering (VT-SWAXS) studies

To analyze the SCO behavior of powder samples of **1** and **2**, differential scanning calorimetry (DSC) and small- and wide-angle X-ray scattering (SWAXS) studies were carried out. DSC measurements were performed to get insights into the phase, enthalpy (ΔH), and entropy (ΔS) changes associated with the SCO of the complexes. A heat flow versus T plot of the powder sample of **1** showed peaks in the heating ($T1 = 299$ K) and cooling ($T1 = 292$ K) modes as depicted in Fig. 3a, whereas powder sample of **2** showed peaks $T1 = 304$ K and $T1 = 296$ K as depicted in Fig. 3b. These transition temperatures match well with the $T_{1/2}$ values obtained from SQUID measurements.
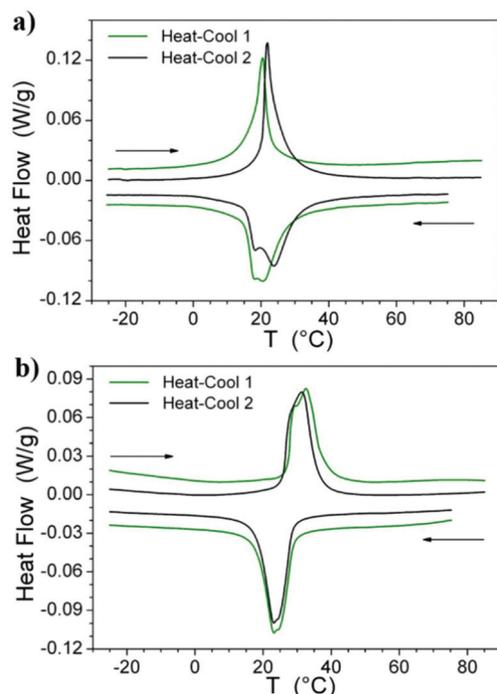
Fig. 3 DSC curves for the powder forms of (a) **1** and (b) **2**, the first two scans are shown (scan rate = 2 °C min⁻¹).

The observed difference between the first and second cycles for **1** and **2** is tentatively attributed to a possible structural reorganization in the crystal lattice as previously reported for **3**. Subsequent cycling resulted in stabilized thermal behaviour as of cycle 2. The ΔH and ΔS values of **1** and **2** obtained from the DSC analyses are in the range observed for iron(II)-SCO complexes (ΔH = 3–27 kJ mol⁻¹ and ΔS = 22–94 J K⁻¹ mol⁻¹). The entropy variation associated with the SCO is primarily due to electronic (ΔS_{elec}) and vibrational (ΔS_{vib}) entropy contributions. The electronic entropy variation—ΔS_{elec} = 13.38 J K⁻¹ mol⁻¹—arises from spin-multiplicity change associated with the LS → HS switching. Intramolecular and intermolecular vibrational modes contribute to ΔS_{vib}. Thus, the excess entropies of 31.72 J K⁻¹ mol⁻¹ (**1**) and 19.32 J K⁻¹ mol⁻¹ (**2**) obtained for the complexes are primarily due to vibrational entropy change between the LS and HS states of **1** and **2**. On a com-

parative scale, previously reported complex **3** showed greater entropy variation (see Table 2) associated with the SCO relative to **1** and **2**. Tentatively, this might come from more significantly affected molecular geometry, ligand planes being somewhat twisted in the LS-complex **3**, but almost orthogonal in **1** as in the model HS-complex **6** (*vide infra*).

In any event, the ΔS values discussed above, obtained using the relation $\Delta S = \Delta H/T$, is correct only for non-cooperative systems. An assessment of ΔS incorporating cooperative intermolecular interactions could be performed by fitting the SCO profiles with Slichter–Drickamer (S–D) model.[84] A good fit of the cooling branch of $\chi_M T$ versus T profile is obtained for **3** (Fig. S8†); the quality of the fits are less satisfactory for complexes **1** and **2** (Fig. S6 and S7†), most probably due to the gradual HS → LS switching associated with the complexes below ~300 K. Cooperativity parameters (Γ/kJ mol⁻¹) of 5, 7.2, and 9.7 are obtained for complexes **1**, **2**, and **3**, respectively; the higher value of Γ obtained for **3** corroborate well with the abrupt SCO associated with the complex.

To further investigate the structural reorganization associated with the SCO in **1** and **2**, SWAXS studies were carried out. From the data depicted in Fig. 4 and 5, the medium and wide-angle ranges of the SWAXS patterns of **1** and **2** reversibly change between the LS and HS states, as the different geometries of the complexes in their corresponding LS and HS states modify the molecular arrangement upon spin-state switching.

These structural changes appeared to be fully reproducible and reversible on crossing several times between the LS and HS states of **1** and **2** analogues to the previously reported complex **3**. Overall, the SWAXS patterns of the complexes reveal the stable and reproducible SCO behavior of the complexes.

Density functional theory (DFT) studies

The relative stability of the HS and LS states of the complexes **1**, **2**, **3**, and **4** were studied by DFT computations in gas-phase, and the results are compared with the available experimental data to get insights into the role of ligand electronic substituent in altering SCO. The internal energy at the HS and LS states computed at their structural minima represents the "electronic contribution" to enthalpy (ΔH_{elec}). In this approach, a larger gap between energy minima delays the SCO

Table 2 Thermodynamic parameters associated with SCO of the complexes **1**, **2**, and **3**

Parameter	1		2		3	
	SQUID	DSCᵃ	SQUID	DSCᵃ	SQUID	DSCᵃ
T_1^{up} (K)	299	298	304	304.4	348.9	347.1
T_1^{down} (K)	292	295ᵇ	299	296.2ᵇ	346.3	344.4ᵇ
ΔT (K)	7	3	5	8.15	2.6	2.7
ΔH (kJ mol⁻¹)		13.4ᵃ (11)ᶜ		9.8 (13.5)		19.8 (12)
ΔS (J K⁻¹ mol⁻¹)		45.1ᵃ (37.1)ᶜ		32.7 (45)		57.2 (34.5)

ᵃ From the second cycle. ᵇ Discrepancies between the T values obtained from SQUID and DSC could have arisen due to the slightly different phase transition kinetics associated with the samples used for the SQUID and DSC measurements. ᶜ Values obtained by fitting the $\chi_M T$ versus T plots with S-D model.
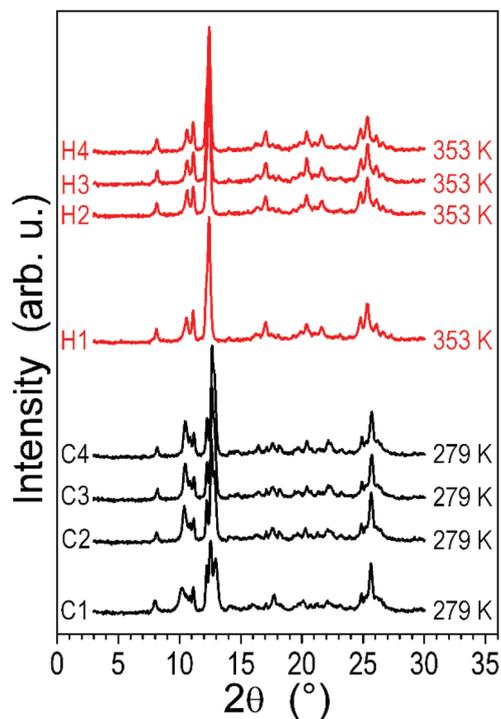
Fig. 4 Variable temperature SWAXS patterns of **1** in powder form. The notations Cn (n = 1–4) and Hn (n = 1–4) represent crystalline states after the nth heating or cooling cycle associated with the HS state (red curves and labels) and LS state (black), respectively, at indicated temperature of patterns.
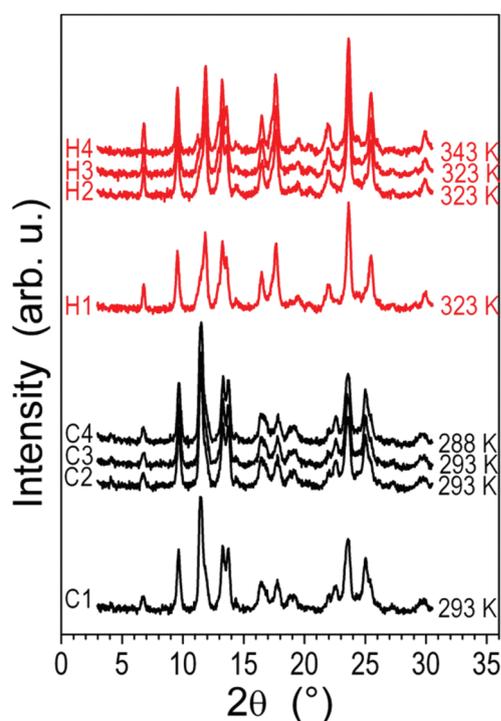
Fig. 5 Variable temperature SWAXS patterns of **2** in powder form. The notations Cn (n = 1–4) and Hn (n = 1–4), labels and colours are as defined in Fig. 4.

to a higher temperature, as higher entropy term $T\Delta S$ needs to be reached at transition. All things being otherwise equal, such DFT calculations should therefore follow the trend in transition temperatures ($T_{1/2}$). The effect of the ligand modification on the ligand-field splitting is evaluated through the computation of Δ_O for the LS minima.

Notice that Δ_O corresponds to the energy difference between the antibonding e_g and non-bonding t_{2g} sets of orbitals in an octahedral compound. Despite the loss of octahedral symmetry in the actual molecules, for simplicity, we will maintain the orbital notation. The magnitude of Δ_O is occasionally considered of prime importance in shaping ΔH_{elec} when other effects such as intra- or intermolecular interactions are not relevant. In the present case, the studied complexes differ in the functional groups located in the distal position, far away from the coordinating pyrazole, tetrazole, and pyridine nitrogens. Therefore, the complexes are suitable for a study of the ligand-field splitting in gas-phase conditions. Modelling of complexes **1** to **4** thereby led to molecular conformations in HS and LS states in well agreement with results from single crystal X-ray diffraction. In particular, the average Fe–N bond-lengths in the LS states coincides within 0.01 Å with experimental values and discrepancies with model HS-complex **6** are only of 0.01–0.03 Å (Tables 3 and 1). Fe–N bonding strengths are thus correctly implemented in our modelling, otherwise leading to distortion parameters Σ in LS states within 5° from effective values. Based on these validated model conformations, computations revealed larger ΔH_{elec} values for **3** and **4** (see Table 3), which implies a larger $T_{1/2}$ and therefore agrees with the high transition temperature found experimentally for **3** (~347 K), and predominantly LS state of **4** up to 385 K.

In turn, the ΔH_{elec} values of **1** and **2** are smaller than the values obtained for **3** and **4** and comparable to each other, in agreement with their measured transition temperatures (295 K (**1**) *versus* 301 K (**2**)). It thus follows that the predicted ΔH_{elec} and $T_{1/2}$ values capture the trend of the experimental SCO behavior. That being said, the $T_{1/2}$ values are clearly overestimated by our computational method, which is probably due to (i) the usual error associated with the evaluation of ΔH_{elec} with the current electronic structure method (PBE+U+D2 has a mean absolute error of 4.4 kJ mol^{-1}), and above all (ii) to the contribution of crystal packing, (notice that an enthalpy difference of 5 kJ mol^{-1} would translate into a 100 K difference in $T_{1/2}$).

The ligand-field splitting is analysed by looking at the energy of the t_{2g} and e_g orbitals as discussed above. Notice that only the average orbital energy is considered and not the further fine-structure splitting due to the loss of octahedral symmetry. Within the t_{2g} set, the d_{yz} and d_{xz} orbitals appear lower in energy, followed by d_{xy}, which is also the HOMO (Fig. S9 and S10†). The first six unoccupied orbitals are π-orbitals that are mainly localized in the pyridine ring and have some Fe contribution. Soon after, one finds the e_g set: first the d_{z^2} and later the $d_{x^2-y^2}$ orbital, slightly separated in energy. The value of Δ_O is calculated using the average energy of each set (see Table 4 and Fig. S9†).

Table 3 Average values of Fe–N bond length ($\bar{d}$(Fe–N)) and distortion parameter (Σ) in the LS and HS states determined from the gas-phase minima of **1**, **2**, **3** and **4**, electronic enthalpy difference (Δ_{Helec}) between their LS ($S = 0$) and HS ($S = 2$) spin states minima and predicted $T_{1/2}$

	HS		LS			
	$\bar{d}$(Fe–N)/Å	Σ/°	$\bar{d}$(Fe–N)/Å	Σ/°	ΔH_{elec}/kJ mol^{-1}	$T_{1/2}$/K
1	2.188	166.37	1.944 (1.94(7))[a]	87.86	31.5	459
2	2.189	157.97	1.950	88.63	30.8	447
3	2.184 (2.16(3))[a]	164.26	1.941 (1.93(3))[a]	87.33	36.5	534
4	2.175	161.37	1.935 (1.93(8))[a]	85.34	36.3	531

$\Sigma = \sum_{i}^{12}|90 - \alpha_i|$, where α are the twelve *cis*-N–Fe–N angles around the Fe atom. [a] Experimental values obtained from X-ray structural analysis.

Table 4 The average energy of the two sets of 3d-orbitals for compounds **1**, **2**, **3**, and **4**, the energy difference between them (that is, Δ_O) and electronic enthalpy—ΔH_{elec}. The Fermi energy is set at zero

	1	2	3	4
t_{2g}/eV	−1.30	−1.29	−1.12	−1.13
e_g/eV	2.48	2.47	2.68	2.68
Δ_O/eV	3.78	3.77	3.80	3.81
Δ_O/kJ mol^{-1}	365.5	364.2	367.6	367.8
ΔH_{elec}/kJ mol^{-1}	31.5	30.8	36.5	36.3

The results are clearly different for the two sets of compounds: **1** and **2** have Δ_O values of 3.78 eV and 3.77 eV, respectively, whereas those with –COOR ligands (**3** and **4**) have Δ_O values of 3.80 eV and 3.81 eV, respectively (note, 0.01 eV = ~116 K). It thus follows that the ligand field splitting is smaller in the former than in the latter set of complexes. Such difference in the ligand field splitting is in excellent agreement with the trend in ΔH_{elec} values discussed above. The –COOR (R = –CH$_3$ or –C$_2$H$_5$) electron-withdrawing group induced back-bonding interaction with the Fe-centre, thus increasing the ligand-field splitting, which leads to an SCO transition at higher temperatures. Interestingly, the computations also reproduce the experimentally observed shorter Fe–N bond distances (see Tables 1 and 3) in the –COOR series of complexes evidencing the ability of these ligands, L^{3}H and L^{4}H, for better π-back bonding interaction with the metal. In the literature, confirmation of such substituent induced ligand field modulation and the associated $T_{1/2}$ variation is obtained by studying spin-state switching behavior in solution phase.[30] Unfortunately, a significant problem we faced during this study is the sluggish solubility of the complexes in common organic solvents and in binary solvent mixtures such as dichloromethane/methanol. Though the complexes showed appreciable solubility in dimethyl sulfoxide (DMSO), complete solubilization was not realized, prohibiting detailed solution-phase magnetic measurements based on the Evans method.[85]

Functionalization of the parent SCO complex **1** with substituents modulated the SCO by imparting additional electronic effects and intermolecular interactions between the switching entities. For example, many complexes featuring substituents capable of hydrogen bonding interactions showed cooperative SCO attributed to hydrogen bond mediated elastic interactions.[3,86] On the other hand, tethering bulky substituents with switching cores either block the SCO or effect gradual spin-state switching due to steric effects. The ~6 K increase in $T_{1/2}$ observed for **2** ($T_{1/2}$ = ~301 K) relative to **1** ($T_{1/2}$ = ~295 K) thus tentatively, in the absence of X-ray structure for **2**, relates to the different distribution of switching entities in the crystallographic cells. On the other hand, the gradual onset of SCO in **5** is a testimony of bulky pyrene substituent mediated blocking of SCO *via* steric interactions as previously reported for [Fe(bpp)$_2$]$^{2+}$ complexes.[87] In any event, some change of SCO behaviour for **5** was fatal, since the molecular self-assembly is deeply modified relative to **1** and **3** and yields a crystalline structure with lamellar character and disordered interlayers. Further, complexes **1** and **2** showed a less abrupt $\chi_m T$ jump compared to the rather abrupt SCO characteristics of **4**, evidencing the coupling between SCO and intermolecular interactions. The absence of SCO in lattice solvent-free crystals of **3** and **4** is a proof of rigid lattice or strong intermolecular contacts inhibiting structural reorganization from LS → HS state. Note that the solvent-free crystalline form of **3** reported by us is light-induced excited spin state trapping (LIESST) inactive, whereas its microcrystalline counterpart showed LIESST effect, evidencing strong intermolecular interactions prohibiting the SCO in **3**.[75] Thus we believe that the presence of lattice solvent molecules (Fig. S12†) and less dense molecular organization in the crystalline form of **1** and powder forms of **1**, **2**, and **3** facilitated SCO. However, the lack of suitable intermolecular contacts between switching cores in the crystalline structure of pyrene tethered complex **5** rendered SCO gradual.

Spin-crossover also depends on ligand field strength around Fe(ɪɪ) centres. Consequently, attempts to engineer SCO *via* chemical means by tailoring a parent SCO entity with electron-withdrawing and electron-donating groups have been made successfully, especially in the solution phase.[23–25,27–31] To facilitate an understanding of the role of electronic structure modification in tuning SCO characteristics of complexes **1**, **2**, **3**, and **4**, experimentally obtained thermodynamics parameters of the complexes **1**, **2**, **3** are compared with the values obtained from DFT studies. DFT calculations estimated higher $T_{1/2}$ values for **3** and **4** relative to **1** and **2**, as shown in Table 3, which is consistent with the experimentally observed trend (Table 2). The electron-withdrawing (EW) groups lower the

energy of ligand-based π^* molecular orbitals (MOs), thereby increasing the conjugation between ligand and metal-centred t_{2g} orbitals facilitating metal–ligand back-bonding (d-π^*) interaction. Interestingly, this line of analysis is in excellent agreement with the report by Kaizaki and co-workers detailing the role of pyridyl substituent in altering $T_{1/2}$ values in [Fe(NCE)$_2$(PyR)$_2$(μ-bpypz)$_2$] complex systems.[23] Their arguments in favour of EW group induced increase in $T_{1/2}$ also holds true for the –COOR series of complexes studied in this work. Moreover, recent solution-phase studies of the closely resembling [Fe(R-bpp)$_2$]$^{2+}$ complexes by Halcrow and co-workers[29] also noticed d-π^* bonding mediated increase of switching temperature. Remarkably, if we were to group $T_{1/2}$ values in [Fe(R-bpp)$_2$]$^{2+}$ systems, most complexes substituted with –COOR groups at the 4-position of the pyridine ring showed SCO at high temperature relative to the parent [Fe(bpp)$_2$](BF$_4$)$_2$ with $T_{1/2}$ = 253 K. However, the above arguments are not applicable for distorted systems, especially for [Fe(R-bpp)$_2$]$^{2+}$ complexes, whose SCO behavior are primarily determined by angular parameters rather than by substituent effects: a pronounced distortion kinetically traps the HS state and inhibits SCO. In this line, the close to ideal octahedral geometry and charge-neutral characteristic of [Fe(R-ptp)$_2$]^0 complexes might be an explanation for the observed higher $T_{1/2}$ in **3** relative to **1** and **2** on the basis of ligand field strength. By the virtue of the computational proofs scrutinizing the SCO properties variation in this [Fe(R-ptp)$_2$]^0 series and of the combinations with other reports detailing similar observations, we stress that the ligand-based electronic effects are of significance in modulating SCO characteristics in solid-state along with intermolecular interactions. The ligand-field aspect should be considered while designing SCO complexes.

Conclusions

By synthesizing complexes **1–5** in powder and crystalline forms, the role of intermolecular interactions in affecting SCO in [Fe(R-ptp)$_2$]^0 family of complexes is elucidated. The coordination environment around the iron(II) in LS-[Fe(R-ptp)$_2$]^0 complexes is close to the ideal octahedral geometry expected for such six-coordinate complexes. Remarkably, the SCO in complexes **1**, **2**, and **3** is cooperative, hysteretic, and reversible as inferred from SQUID, DSC, and SWAXS measurements. Moreover, a judicious ligand designing strategy has been invoked to attempt SCO programming in the charge-neutral complexes. A simple variation of the nature of the electronic substituent at the 4-position of the pyridine ring of ptp skeleton from R = H/CH$_2$OH to COOR favoured LS state in COOR series of complexes—**3** and **4**—around RT. DFT calculations evidence the electronic substituent effects governing $T_{1/2}$ in complexes **1**, **2**, **3**, and **4** by predicting greater enthalpy change and increased $T_{1/2}$ value for the COOR substituted complexes compared with **1** and **2**. Overall, the results presented in this study are encouraging towards the ligand structure mediated pre-synthesis tuning of SCO temperature with consequences

towards the realization of molecular electronic/spintronic devices based on bi-stable SCO complexes.

Conflicts of interest

There are no conflicts to declare.

Acknowledgements

References

1 J. Krober, E. Codjovi, O. Kahn, F. Groliere and C. Jay, *J. Am. Chem. Soc.*, 1993, **115**, 9810–9811.

2 L. Zhang, G.-C. Xu, H.-B. Xu, T. Zhang, Z.-M. Wang, M. Yuan and S. Gao, *Chem. Commun.*, 2010, **46**, 2554.

3 B. Weber, W. Bauer and J. Obel, *Angew. Chem., Int. Ed.*, 2008, **47**, 10098–10101.

4 O. Iasco, E. Rivière, R. Guillot, M. Buron-Le Cointe, J.-F. Meunier, A. Bousseksou and M.-L. Boillot, *Inorg. Chem.*, 2015, **54**, 1791–1799.

5 H. Hagiwara, T. Masuda, T. Ohno, M. Suzuki, T. Udagawa and K. Murai, *Cryst. Growth Des.*, 2017, **17**, 6006–6019.

6 B. Schäfer, C. Rajnák, I. Šalitroš, O. Fuhr, D. Klar, C. Schmitz-Antoniak, E. Weschke, H. Wende and M. Ruben, *Chem. Commun.*, 2013, **49**, 10986.

7 I. Šalitroš, N. T. Madhu, R. Boča, J. Pavlik and M. Ruben, *Monatsh. Chem.*, 2009, **140**, 695–733.

8 M. A. Halcrow, *Chem. Lett.*, 2014, **43**, 1178–1188.

9 E. Tailleur, M. Marchivie, N. Daro, G. Chastanet and P. Guionneau, *Chem. Commun.*, 2017, **53**, 4763–4766.

10 S. Decurtins, P. Gütlich, C. P. Köhler, H. Spiering and A. Hauser, *Chem. Phys. Lett.*, 1984, **105**, 1–4.

11 A. Hauser, in *Spin Crossover in Transition Metal Compounds II*, Springer Berlin Heidelberg, Berlin, Heidelberg, 2004, vol. 234, pp. 155–198.

12 C. Lefter, V. Davesne, L. Salmon, G. Molnár, P. Demont, A. Rotaru and A. Bousseksou, *Magnetochemistry*, 2016, **2**, 18.

13 C. Lefter, S. Rat, J. S. Costa, M. D. Manrique-Juárez, C. M. Quintero, L. Salmon, I. Séguy, T. Leichle, L. Nicu, P. Demont, A. Rotaru, G. Molnár and A. Bousseksou, *Adv. Mater.*, 2016, **28**, 7508–7514.

14 V. Shalabaeva, K. Ridier, S. Rat, M. D. Manrique-Juarez, L. Salmon, I. Séguy, A. Rotaru, G. Molnár and A. Bousseksou, *Appl. Phys. Lett.*, 2018, **112**, 013301.

15 A. Rotaru, I. A. Gural'skiy, G. Molnár, L. Salmon, P. Demont and A. Bousseksou, *Chem. Commun.*, 2012, **48**, 4163–4165.

16 E. Ruiz, *Phys. Chem. Chem. Phys.*, 2014, **16**, 14–22.

17 K. Senthil Kumar and M. Ruben, *Coord. Chem. Rev.*, 2017, **346**, 176–205.

18 M. Ruben, E. Breuning, J.-M. Lehn, V. Ksenofontov, F. Renz, P. Gütlich and G. B. M. Vaughan, *Chem. – Eur. J.*, 2003, **9**, 4422–4429.

19 F. Prins, M. Monrabal-Capilla, E. A. Osorio, E. Coronado and H. S. J. van der Zant, *Adv. Mater.*, 2011, **23**, 1545–1549.

20 O. Kahn, *Science*, 1998, **279**, 44–48.

21 *Spin-crossover materials: properties and applications*, ed. M. A. Halcrow, Wiley, Chichester, West Sussex, United Kingdom, 2013.

22 *Spin crossover in transition metal compounds*, ed. P. Gütlich and H. A. Goodwin, Springer, Berlin, New York, 2004.

23 K. Nakano, N. Suemura, K. Yoneda, S. Kawata and S. Kaizaki, *Dalton Trans.*, 2005, 740.

24 J. G. Park, I.-R. Jeon and T. D. Harris, *Inorg. Chem.*, 2015, **54**, 359–369.

25 S. Furukawa, Y. Hitomi, T. Shishido, K. Teramura and T. Tanaka, *J. Phys. Chem. A*, 2011, **115**, 13589–13595.

26 M. Halcrow, *Crystals*, 2016, **6**, 58.

27 J. N. McPherson, R. W. Hogue, F. S. Akogun, L. Bondì, E. T. Luis, J. R. Price, A. L. Garden, S. Brooker and S. B. Colbran, *Inorg. Chem.*, 2019, **58**, 2218–2228.

28 A. Kimura and T. Ishida, *ACS Omega*, 2018, **3**, 6737–6747.

29 L. J. Kershaw Cook, R. Kulmaczewski, R. Mohammed, S. Dudley, S. A. Barrett, M. A. Little, R. J. Deeth and M. A. Halcrow, *Angew. Chem., Int. Ed.*, 2016, **55**, 4327–4331.

30 S. Rodríguez-Jiménez, M. Yang, I. Stewart, A. L. Garden and S. Brooker, *J. Am. Chem. Soc.*, 2017, **139**, 18392–18396.

31 I. Prat, A. Company, T. Corona, T. Parella, X. Ribas and M. Costas, *Inorg. Chem.*, 2013, **52**, 9229–9244.

32 A. Kimura and T. Ishida, *Inorganics*, 2017, **5**, 52.

33 P. Gütlich, A. Hauser and H. Spiering, *Angew. Chem., Int. Ed. Engl.*, 1994, **33**, 2024–2054.

34 M. A. Halcrow, *Chem. Soc. Rev.*, 2011, **40**, 4119.

35 S. Brooker, *Chem. Soc. Rev.*, 2015, **44**, 2880–2892.

36 E. Collet and P. Guionneau, *C. R. Chim.*, 2018, **21**, 1133–1151.

37 B. Weber and F. A. Walker, *Inorg. Chem.*, 2007, **46**, 6794–6803.

38 P. N. Martinho, Y. Ortin, B. Gildea, C. Gandolfi, G. McKerr, B. O'Hagan, M. Albrecht and G. G. Morgan, *Dalton Trans.*, 2012, **41**, 7461.

39 M. Milek, F. W. Heinemann and M. M. Khusniyarov, *Inorg. Chem.*, 2013, **52**, 11585–11592.

40 S. G. Telfer, B. Bocquet and A. F. Williams, *Inorg. Chem.*, 2001, **40**, 4818–4820.

41 J. A. Real, A. B. Gaspar, V. Niel and M. C. Muñoz, *Coord. Chem. Rev.*, 2003, **236**, 121–141.

42 M. Nihei, T. Shiga, Y. Maeda and H. Oshio, *Coord. Chem. Rev.*, 2007, **251**, 2606–2621.

43 M. Nishino, K. Boukheddaden, Y. Konishi and S. Miyashita, *Phys. Rev. Lett.*, 2007, **98**, 247203.

44 M. M. Dîrtu, C. Neuhausen, A. D. Naik, A. Rotaru, L. Spinu and Y. Garcia, *Inorg. Chem.*, 2010, **49**, 5723–5736.

45 C. Bartual-Murgui, S. Vela, M. Darawsheh, R. Diego, S. J. Teat, O. Roubeau and G. Aromí, *Inorg. Chem. Front.*, 2017, **4**, 1374–1383.

46 C. Bartual-Murgui, S. Vela, O. Roubeau and G. Aromí, *Dalton Trans.*, 2016, **45**, 14058–14062.

47 G. D'Avino, A. Painelli and K. Boukheddaden, *Phys. Rev. B*, 2011, **84**, 104119.

48 H. Spiering, T. Kohlhaas, H. Romstedt, A. Hauser, C. Bruns-Yilmaz, J. Kusz and P. Gütlich, *Coord. Chem. Rev.*, 1999, **190–192**, 629–647.

49 J. Tao, R.-J. Wei, R.-B. Huang and L.-S. Zheng, *Chem. Soc. Rev.*, 2012, **41**, 703–737.

50 M. Marchivie, P. Guionneau, J.-F. Létard and D. Chasseau, *Acta Crystallogr., Sect. B: Struct. Sci., Cryst. Eng. Mater.*, 2003, **59**, 479–486.

51 A. B. Koudriavtsev and W. Linert, *J. Struct. Chem.*, 2010, **51**, 335–365.

52 H. S. Scott, R. W. Staniland and P. E. Kruger, *Coord. Chem. Rev.*, 2018, **362**, 24–43.

53 J. Olguín and S. Brooker, *Coord. Chem. Rev.*, 2011, **255**, 203–240.

54 B. Weber, W. Bauer, T. Pfaffeneder, M. M. Dîrtu, A. D. Naik, A. Rotaru and Y. Garcia, *Eur. J. Inorg. Chem.*, 2011, **2011**, 3193–3206.

55 M. Hostettler, K. W. Törnroos, D. Chernyshov, B. Vangdal and H.-B. Bürgi, *Angew. Chem., Int. Ed.*, 2004, **43**, 4589–4594.

56 Z. Arcis-Castíllo, S. Zheng, M. A. Siegler, O. Roubeau, S. Bedoui and S. Bonnet, *Chem. – Eur. J.*, 2011, **17**, 14826–14836.

57 M. A. Halcrow, *Chem. Commun.*, 2013, **49**, 10890.

58 A. Galet, M. C. Muñoz, V. Martínez and J. A. Real, *Chem. Commun.*, 2004, 2268–2269.

59 Y.-H. Luo, C. Chen, G.-W. Lu, D.-L. Hong, X.-T. He, C. Wang, J.-Y. Wang and B.-W. Sun, *J. Phys. Chem. Lett.*, 2018, **9**, 7052–7058.

60 T. Kosone, Y. Makido, S. Okuda, A. Haigo, T. Kawasaki, D. Akahoshi, T. Saito and T. Kitazawa, *Crystals*, 2019, **9**, 370.

61 K. S. Kumar, M. Studniarek, B. Heinrich, J. Arabski, G. Schmerber, M. Bowen, S. Boukari, E. Beaurepaire, J. Dreiser and M. Ruben, *Adv. Mater.*, 2018, **30**, 1705416.

62 S. Zaiter, C. Kirk, M. Taylor, Y. M. Klein, C. E. Housecroft, N. F. Sciortino, J. E. Clements, R. I. Cooper, C. J. Kepert and S. M. Neville, *Dalton Trans.*, 2019, **48**, 7337–7343.

63 S. Vela, J. J. Novoa and J. Ribas-Arino, *Phys. Chem. Chem. Phys.*, 2014, **16**, 27012–27024.

64 A. V. Kazakova, A. V. Tiunova, D. V. Korchagin, G. V. Shilov, E. B. Yagubskii, V. N. Zverev, S. C. Yang, J. Lin, J. Lee, O. V. Maximova and A. N. Vasiliev, *Chem. – Eur. J.*, 2019, **25**, 10204–10213.

65 D. L. Reger, J. R. Gardinier, M. D. Smith, A. M. Shahin, G. J. Long, L. Rebbouh and F. Grandjean, *Inorg. Chem.*, 2005, **44**, 1852–1866.

66 S. Rat, K. Ridier, L. Vendier, G. Molnár, L. Salmon and A. Bousseksou, *CrystEngComm*, 2017, **19**, 3271–3280.

67 D. Shao, L. Shi, F.-X. Shen, X.-Q. Wei, O. Sato and X.-Y. Wang, *Inorg. Chem.*, 2019, **58**, 11589–11598.

68 I. Šalitroš, J. Pavlik, R. Boča, O. Fuhr, C. Rajadurai and M. Ruben, *CrystEngComm*, 2010, **12**, 2361.

69 P. D. Southon, L. Liu, E. A. Fellows, D. J. Price, G. J. Halder, K. W. Chapman, B. Moubaraki, K. S. Murray, J.-F. Létard and C. J. Kepert, *J. Am. Chem. Soc.*, 2009, **131**, 10998–11009.

70 R. G. Miller and S. Brooker, *Chem. Sci.*, 2016, **7**, 2501–2505.

71 W. Huang, F. Shen, M. Zhang, D. Wu, F. Pan and O. Sato, *Dalton Trans.*, 2016, **45**, 14911–14918.

72 M. Fumanal, F. Jiménez-Grávalos, J. Ribas-Arino and S. Vela, *Inorg. Chem.*, 2017, **56**, 4474–4483.

73 T. Miyamachi, M. Gruber, V. Davesne, M. Bowen, S. Boukari, L. Joly, F. Scheurer, G. Rogez, T. K. Yamada, P. Ohresser, E. Beaurepaire and W. Wulfhekel, *Nat. Commun.*, 2012, **3**, 938.

74 K. S. Kumar and M. Ruben, *Angew. Chem., Int. Ed.*, DOI: 10.1002/anie.201911256.

75 K. Senthil Kumar, I. Šalitroš, B. Heinrich, O. Fuhr and M. Ruben, *J. Mater. Chem. C*, 2015, **3**, 11635–11644.

76 D. Gentili, N. Demitri, B. Schäfer, F. Liscio, I. Bergenti, G. Ruani, M. Ruben and M. Cavallini, *J. Mater. Chem. C*, 2015, **3**, 7836–7844.

77 D. Ghosh, P. Parida and S. K. Pati, *Appl. Phys. Lett.*, 2015, **106**, 193105.

78 K. Senthil Kumar, B. Schäfer, S. Lebedkin, L. Karmazin, M. M. Kappes and M. Ruben, *Dalton Trans.*, 2015, **44**, 15611–15619.

79 E. Burzurí, A. García-Fuente, V. García-Suárez, K. Senthil Kumar, M. Ruben, J. Ferrer and H. S. J. van der Zant, *Nanoscale*, 2018, **10**, 7905–7911.

80 M. A. Halcrow, I. Capel Berdiell, C. M. Pask and R. Kulmaczewski, *Inorg. Chem.*, 2019, **58**, 9811–9821.

81 P. Stock, D. Wiedemann, H. Petzold and G. Hörner, *Inorganics*, 2017, **5**, 60.

82 K. Senthil Kumar, B. Heinrich, S. Vela, E. Moreno-Pineda, C. Bailly and M. Ruben, *Dalton Trans.*, 2019, **48**, 3825–3830.

83 L. J. Kershaw Cook, R. Mohammed, G. Sherborne, T. D. Roberts, S. Alvarez and M. A. Halcrow, *Coord. Chem. Rev.*, 2015, **289–290**, 2–12.

84 C. P. Slichter and H. G. Drickamer, *J. Chem. Phys.*, 1972, **56**, 2142–2160.

85 D. F. Evans, *J. Chem. Soc. Resumed*, 1959, 2003.

86 K. Senthil Kumar, Y. Bayeh, T. Gebretsadik, F. Elemo, M. Gebrezgiabher, M. Thomas and M. Ruben, *Dalton Trans.*, 2019, **48**, 15321–15337.

87 K. S. Kumar, I. Šalitroš, N. Suryadevara, E. Moreno-Pineda and M. Ruben, *Eur. J. Inorg. Chem.*, 2018, **2018**, 5091–5097.